Development of
a Radio Interferometer
Operating at 12GHz
for Education and Research

교육과 연구를 위한
12 GHz 전파 간섭계 개발

2015 년 2 월

서울대학교 대학원

물리 · 천문학부 천문학 전공

한정환

Development of
a Radio Interferometer Operating at 12 GHz for Education and Research,

지도 교수 박 용 선

이 논문을 이학석사 학위논문으로 제출함

20015 년 2 월

서울대학교 대학원

물리 · 천문학부 천문학 전공

한 정 환

한정환의 이학석사 학위논문을 인준함

2015 년 2 월

위 원 장 _____ (인)

부위원장 _____ (인)

위   원 _____ (인)

Abstract

We developed a radio interferometer system operating at 12GHz for educations and possibly for research. The commercial components are usually used for satisfying a low cost strategy, and the driving system is made to resist the strong wind, because the installation site is located near the seaside. The interferometer system consists of three off-axis parabola antennas, whose diameter is 1.8 m. The baselines between antennas are about 4m, 19m, and 20 m, so about 4′ resolution can be acquired. The baseline vectors are accurately measured by using a theodolite, a light wave distance measurement, and GPS (Global Positioning System). The center frequency of the receivers is 12.177 GHz, and the bandwidth is 6 MHz. The receiver is able to observe the methanol line (12.178 GHz) and continuum from the Sun, the Moon, and the Galactic plane. The signals of each receiver are sampled and quantized by the digitizer, and then software correlation is conducted with the developed parallel process program. We succeeded in finding fringes toward the Sun, Moon, Crab Nebula, and Cassiopeia A. By using a Nobeyama solar radio image taken at 17 GHz with a bright spot at the center of solar disk, we tried to calibrate uncertainties involving signal cable length, but it was found to be only partially successful. In order to make images of celestial objects, more careful treatment seems necessary with the use of phase calibrators or with a method similar to self-calibration without the phase calibrator.

Keywords : interferometer, 12 GHz, Education

Student Number : 2012-23106

Contents

1. Introduction

1.1 Research Cases

Since Karl Jansky observed Milky Way in the 1930s, radio astronomy has expanded its influence on Astronomy, but the public, even students and amateur astronomers, do not know well radio astronomy. As an effort to introduce radio astronomy, Haystack Observatory developed Small Radio Telescope (SRT), which is an inexpensive radio astronomy tool kit, to serve as an educational tool for many university or research centers, and it has been a favored tool for education.

Many researchers used SRT for astronomy education, digital signal processing, software development, and data analysis. In addition, some of them tried to use it for teaching interferometer concept, which is a technique to innovatively improve the resolution of a radio telescope. Evarts and Rogers (2005) observed Cygnus A at 2.4 GHz with three SRT, whose baselines are about two 5 m, and 1400 m. After running fitting algorithm and calculation of the observed Cygnus A data, the image could be decomposed into two lobes (Fig. 1), even though the error is larger than expected for position and relative strength cannot be accurately determined. Park et al. (2006) observed the Sun with a semi-VLBI system, which consists of two SRT and whose maximum baseline is 35 m. Although the synthesized image of the Sun could not be acquired due to LO (Local Oscillator) with different frequencies, fringe amplitude as a function of fringe frequency and delays, and eye-fitted visibility amplitude calculated for disk only could be secured. As a follow-up study, they used external reference signal to be shared by two telescopes, and they could synthesize a solar image (Fig. 2) with the

observed amplitude and phase information (Park et al. 2008). In 2006, Very Small Radio Telescope (VSRT) interferometer project was started to develop an inexpensive and portable radio astronomy related tool to purpose to teach science, engineering, mathematics, and astronomy for community college faculty, high school and undergraduate institutions (Arndt and Rogers 2009).
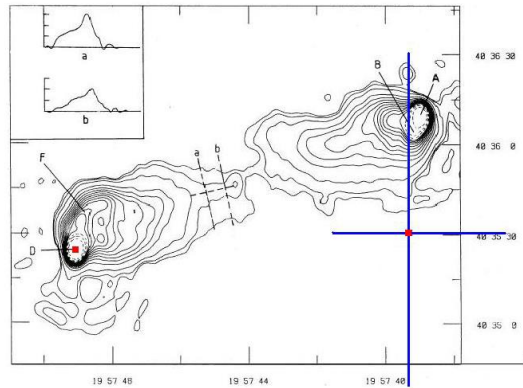

Fig. 1 Cygnus A 2.4 GHz Map from Alexander et al. (1984) with overlay representing results from SRT interferometer (Evarts and Rogers 2005).
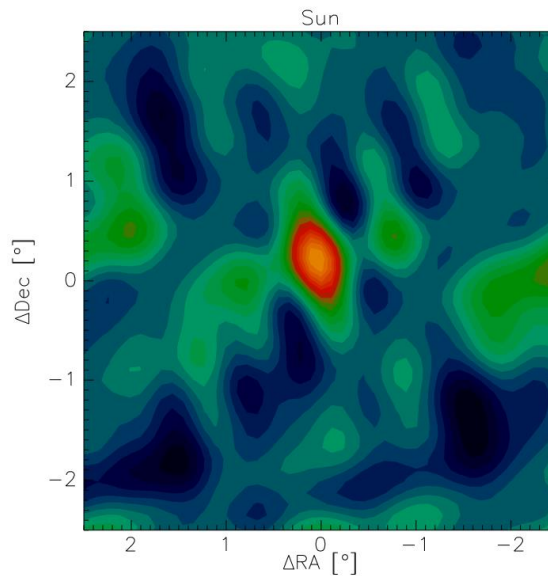

Fig. 2. Synthesized image of the Sun (Park et al. 2008)

1.2 Background of Development

National Youth Space Center (hereafter NYSC) planned to develop the astronomy program to be able to progress in bad weathers or in the daytime. The program with radio telescopes is most proper for this purpose. Since the single radio telescope must have an expensive large diameter dish in order to acquire the images with proper resolution, which can attract young students, interferometer system seems to be a better option than single radio telescope to acquire the image. Seoul National University also wanted to develop interferometer system for educations and researches of (under) graduate students. For the needs of two institutes, the Goheung Interferometer (Radio Interferometer operating at 12 GHz) project could be started by the support of NYSC.

1.3 The Development Purpose and Significance

According to the original plan, the interferometer system must produce the image of the Sun with resolution from 3′ to 4′. Moreover, we planned to develop the system to be able to detect not only continuum, but also line spectrum. Considering all together various factors such as scientific and educational function of the system, fund scale, availability of commercial devices, the size of installation site, receiver sensitivity, etc., we set the input frequency to 12.2GHz. We hope to observe continuously the change of solar activity and make the solar images, as well as make the radio map of 12 GHz type II methanol maser on Galactic plane and monitor their variation (Breen et al. 2012). Other details will be described in the next section. This system will contribute not only to the education of young students who visit the center and (under)

graduate students about interferometer system, but also to the research of the NYSC staffs.

2. Development of System

2.1 Reflector and Antenna Arrangement

Off-axis parabola reflectors (Fig. 3), which are existing commercial products for satellite communication made by High Gain Antenna, are applied to our system. The advantage of this type reflector is enhancing light gathering power by setting a feeder and its supports out of the path of the incoming radio waves. The disadvantages are that an off-axis parabola reflector is more difficult to design and more expensive than typical parabola antennas. However, we bought the commercial products, so these disadvantages do not matter. As shown in the Fig. 3, the reflector diameter is about 2m, and effective diameter is 1.8m (2 x cos(23.7°) ≈ 1.8).
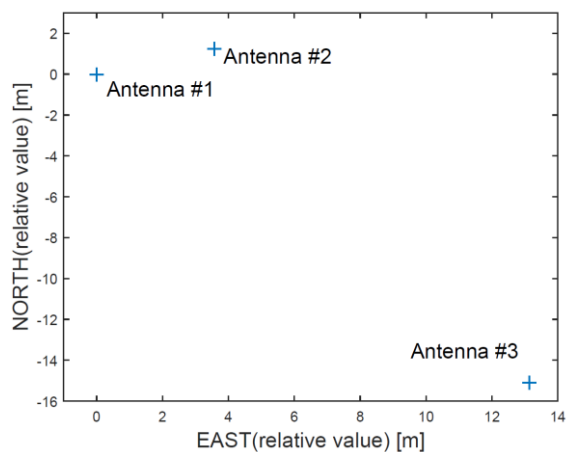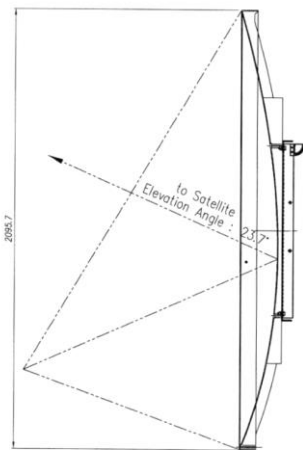

Fig. 3. Off-axis reflector   **Fig. 4.** Arrangement of antennas

We arrange three antennas as shown in Fig. 4. The length between the first antenna and the second antenna is about 20m, the second and the third is about 19m, and the first and the third is about 4m. In order to retain both extended and fine structure in the synthesized image, we secure one short base line and two long base lines. The panorama of the installed antennas is shown in Fig. 5.

Fig. 5. The panorama of Goheung Interferometer

2.2 Development of Driving and Control Systems

2.2.1 Hardware development

We adopt electrical driving and control components with some considerations. First, proper tracking accuracy compared to the image resolution must be achieved. Second, the companies must support well explained manuals and libraries for the development of application programs. The used components with these considerations are listed in Table 1, and the components are installed as shown in Fig. 6.

Table 1. The list of the principal electrical driving and control devices

Component Name	Use	Note	Company
EIP-CPU16B	Standard Ethernet/IP communication CPU module	- Communication with computer - Sending command for motor driving to EIP-M2Q	Ajinextek
EIP-M2Q	Ethernet/IP based Slave 2axes motion function module	- Controlling step motor - Sending pulse and direction signal to step motor - Receiving encoder input and limit signal	Ajinextek
FMA CJ04-AB00	AC Servo Motor		Higen
FDA7004B	Motor Driver	- Controlling the motor - Providing DC to the motor	Higen
S40-6-3600VL	Encoder	- Measuring telescope position - Eliminating an error by a decelerator	Metronix

Fig. 6. Electrical driving and control devices

Mechanical driving and control components (Fig. 7), such as a mount, and a pillar are made by a steel which has strong durability of external shocks, because it is strongly windy in the site where antennas are installed. Gears with precise dimension and low backlash are adopted to achieve a high tracking accuracy. In addition, by adding encoders, the closed loop is made, so high tracking accuracy is achieved.

Fig. 7. Mechanical azimuth (left) and elevation (right) devices

By using these electrical and mechanical components, we can accomplish 0.31 arcsec resolution on the azimuth axis, and 1.62 arcsec resolution on the elevation axis. On the both axes, the servo motor, whose pulse per 1 rotation is 8,000, is used, and the reducer whose reduction gear ratio is 1/100, in front of the motor are installed (Fig. 8). On the elevation axis, 1.62 arcsec (360°/8000/100) resolution is acquired with two devices. On the azimuth axis, the two gears, whose number of teeth is individually 260, and 50, are additionally applied, so their gear ratio is 260/50. Namely, the resolution on azimuth axis is 0.31 arcsec (360°/8000/100/260X50). The explanation is illustrated in Fig. 8. Compared with the systematic accuracy value (15 arcsec will be explained in section 2.2.2) and the minimum resolution of synthesized image (about 4 arcmin), the gear resolution of 1.62 and 0.31 arsecs are good enough.
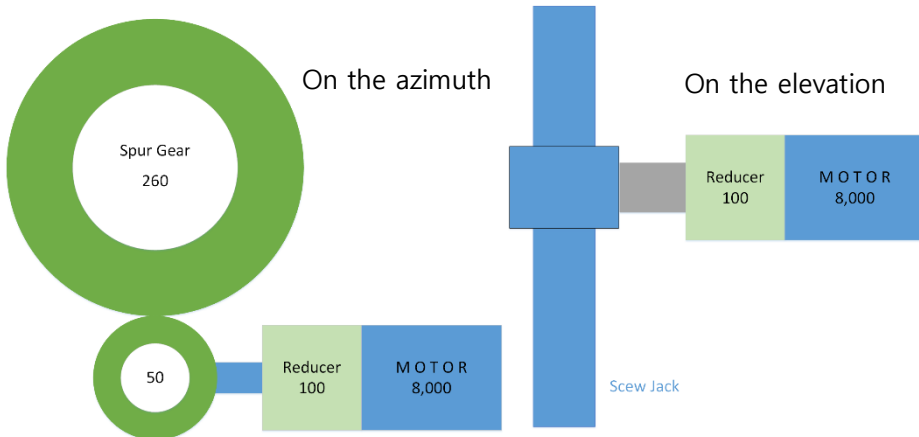

Fig. 8. Schematic of mechanics on the azimuth and elevation

2.2.2 Tracking software development

We adopt a driving and control program, developed by KASI, which is also based on the same components (EIP-CPU18B and EIP-M2Q). We modified some of the program, because the program used by KASI is equatorial type, but our mount is Alt-AZ

type. We apply internal conversion function from equatorial coordinate to azimuth and elevation coordinate. In addition, we removed unnecessary functions, such as the function related to a dome. Our program is a little simpler than the original version.

Tracking accuracy depends on how fast feedback command is arrived and commands are accomplished at the motor. The update period of the motor is configured to 1 sec. 1 sec is the enough value for acquiring a proper tracking accuracy. When the object, whose declination is about 30°, passes the zenith, the object is fastest. The pass length of the object is $\frac{\sqrt{3}}{2}2\pi R$ and the velocity of the object is $\frac{\sqrt{3}}{2}2\pi R/24h$ in length unit. When these values are compared with the values of the object whose declination is 0°, the velocity of the object, whose declination is 30°, in angle unit could be calculated by using proportional expression. Therefore, the fastest velocity at the installed location is about 18.4 arcsec/s ($\frac{\sqrt{3}}{2}$ x 360° x 60arcmin x 60 arcsec/24h/60m/60s). This value is negligible compared with 4 arcmin, the resolution of a synthesized image.
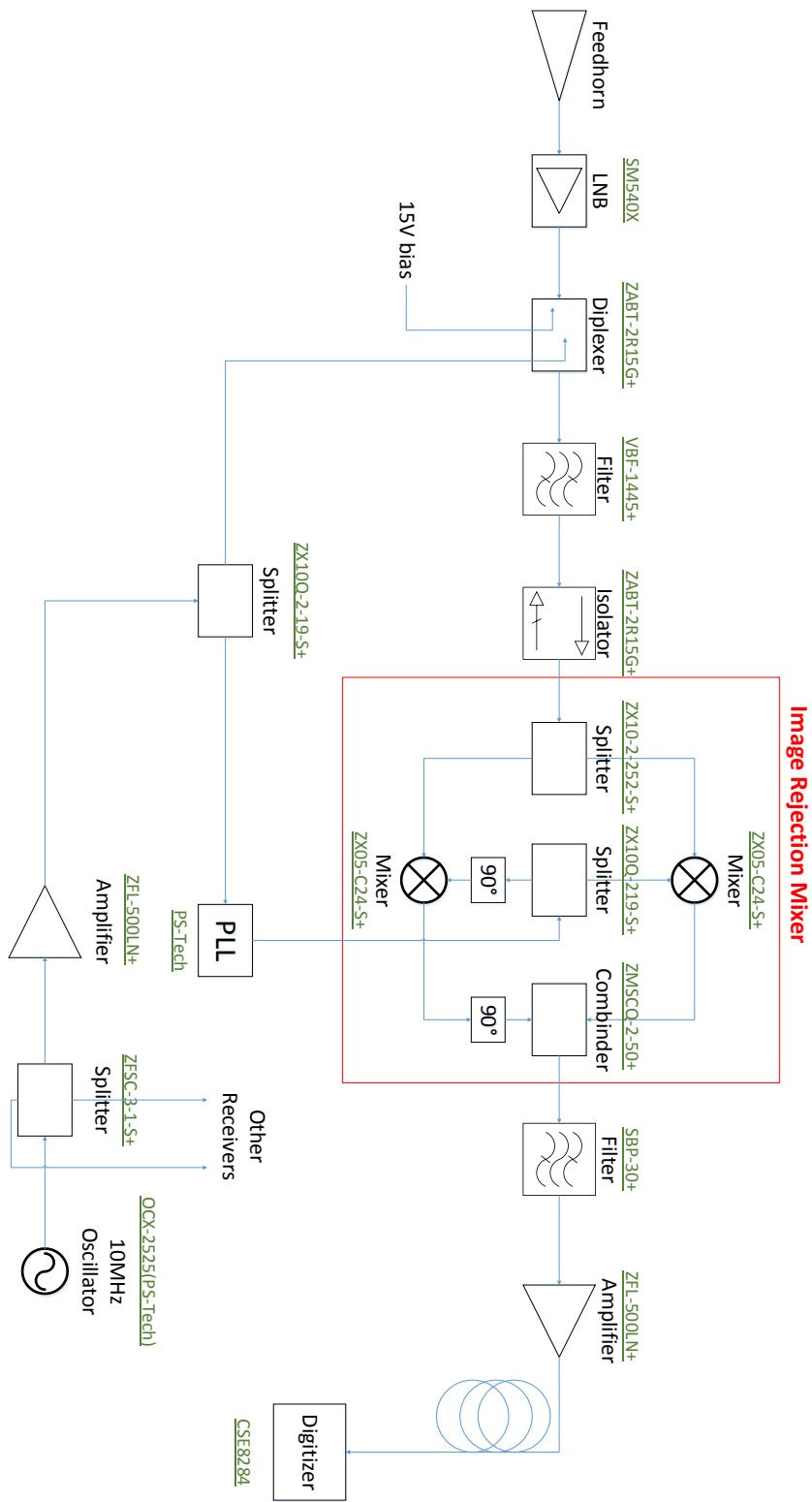

Fig. 9. GUI of the driving and control program

Fig. 10. Block diagram of the receiver

2.3 Development of a Receiver

Fig. 10 shows the block diagram of our receiver. Our receiver (Fig. 11), typical heterodyne system, is designed to detect continuum and methanol line (12.178 GHz). The center frequency is 12.177 GHz, and the bandwidth is about 6 MHz. The input signal is down-converted, with two LO signal, 10.75 GHz, 1397 MHz, to the last IF signal, whose range is from 27 MHz to 33MHz. LNB and PLL in each receivers are coherent to a 10MHz oscillator in the receiver box of the second antenna. In this chapter, the principle devices will be accounted for.
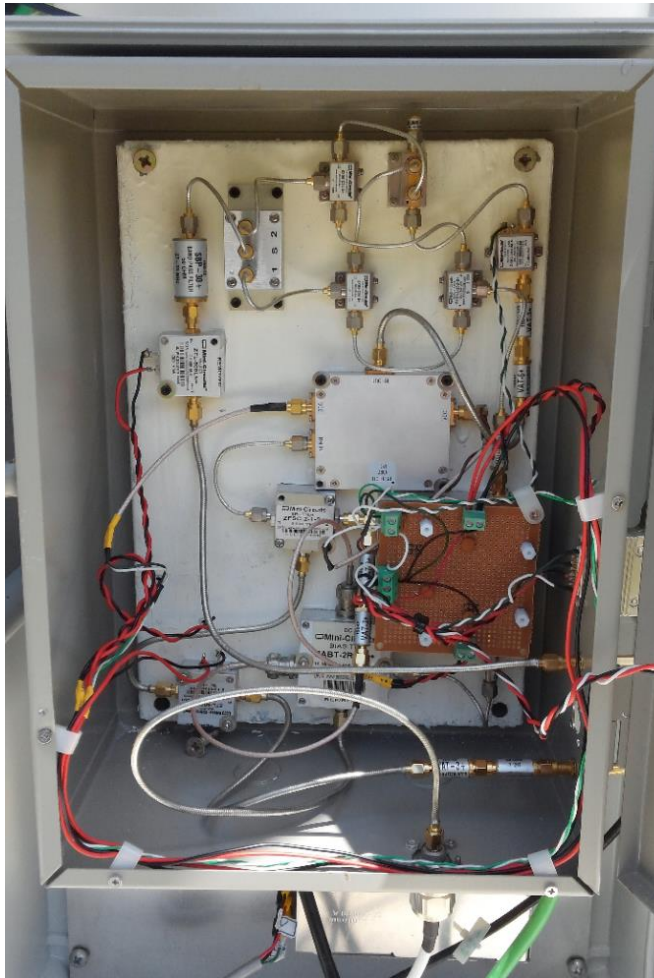

Fig. 11. The inside of the receiver

2.3.1 Low Noise Block down-converter (LNB)

LNB (Fig. 12) is a receiving device to collect radio waves from a reflector. LNB is integrated with a low noise amplifier, a frequency mixer, a PLL, an IF amplifier, and so on. In our system, SM-540X, which is provided by Atron Co., Ltd. is used. Its input frequency range is from 11.7 GHz to 12.2 GHz. External reference input frequency is 10MHz, and LO frequency is 10.75 GHz. Output frequency range is 950 MHz to 1450 MHz. The conversion gain of LNB is 60 dB. Noise figure is 1dB at 25°C.
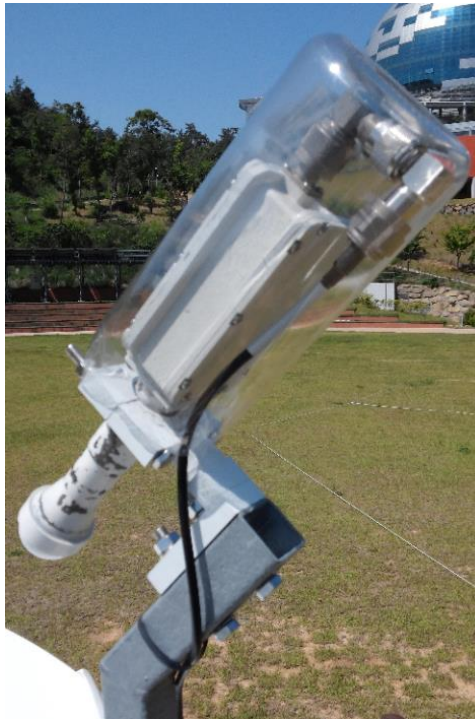

Fig. 12. LNB and feed horn

2.3.2 Diplexer

A diplexer implements frequency domain multiplexing. In our system, the diplexer integrates 15V DC and 10MHz external

reference signal, send them to LNB, and transfers output signal (from 950 MHz to 1450 MHz) from LNB to the receiver.

2.3.3 Realization of image rejection

An image rejection mixer (IRM) is an important device to realize a low noise down-converter by employing phase-cancellation techniques to separate the desired RF signals from the undesired image signals. In our system, we combined several microwave components to realize an image rejection (Fig. 13).

Generally, 90° shifting device is imported after splitting RF signal in many documents, but in our system, the device is imported after splitting local oscillator (LO) signal. Although the block diagram is different compared with the general image rejection mixer, the same effect is performed. The mathematical equations along the signal flow are described in Fig. 13. The used parameters are explained in the caption of Fig. 13.

With a spectrum analyzer, we checked how efficiently the system performs phase-cancellation. When imaginary input signals lower than 1397 MHz are applied, the flat region value of filtered output is about -59 dBm. However, when real input signals higher than 1397 MHz are applied, the value is about -28 dBm. Compared with the values of experiment results, the effect of image rejection is about 30 dB.
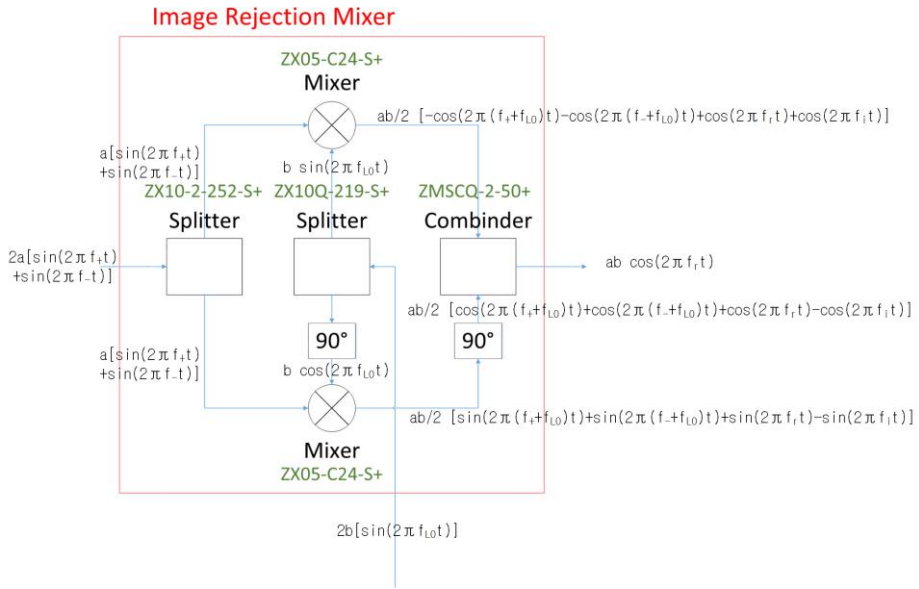
Fig. 13. Realization of image rejection with components. f_r is real output frequency, f_- is imaginary output frequency, f_+ is input frequency related to real output frequency ($f_+ = f_{LO}+f_r$), f_- is input frequency related to real output frequency ($f_- = f_{LO}-f_i$), and f_{LO} is local oscillator frequency.

2.3.4. Phase Locked Loop (PLL)

PLL (Fig. 14) is a control system to generate an output signal, whose phase is coherent to the phase of input signal. PLLs of our system, which are custom-built by PS tech, have 10 MHz input signal, and 1397 MHz output signal. Through these devices, three receivers can be coherent to reference local oscillator 10 MHz.
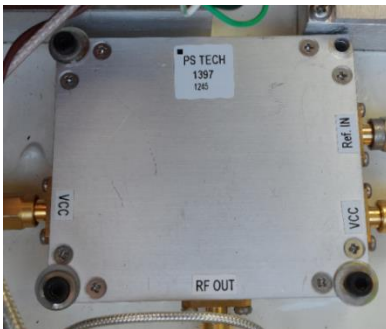

Fig. 14. PLL   **Fig. 15.** Digitizer (CSE 8284)

2.3.5. Digitizer

A digitizer (Fig. 15) is a device to convert from an analog signal value to a digitized signal value. We apply CSE 8284 model made by Gage Instrument. The principal operation properties are summarized in the table 2. The measureable maximum frequency with our digitizer is 25MHz by Nyquist sampling theorem. Although the range of the down-converted input signal is from 27MHz to 33MHz, the original signal (27MHz-33MHz) is reconstructed by using under-sampling theorem. The under-sampling theorem will be account for in the later chapter.

Table 2. The list of the principal digitizer properties

Number of Channels	8
Resolution	12 bits
Sampling rate per channel	1 k, 2k, 5k, 10k, 20k, 50k, 100k, 200k, 500k, 1M, 2M, 5M, 10M, 20M, 25M, 50 M samples / s
Impedance	1MΩ or 50Ω (software-selectable)
Input voltage range	$\pm$ 100mV, $\pm$ 200mV, $\pm$ 500mV, $\pm$1V, $\pm$2V, $\pm$5V, $\pm$10V (in 1MΩ)
Acquisition memory	1 G samples

2.4 The Development of Software Correlator

In order to acquire the visibility, the coherence of the incident waves between pairs of radio antennas (baselines) must be estimated by correlating a sampled representation of the electrical field at each antenna. This work is conducted by the correlator, and there are two types of correlators, a software and a hardware

correlator. In our system, the software correlator seems better than a hardware correlator with some reasons. At first, we can accomplish cross correlation with comparatively low price because current computing commodities, such as PC and networking, which have high competitiveness in performance and price, are well developed. If we had adopted the hardware correlator, we would need to order it with high price. Secondly, the received signal could be massaged by the software correlator. We could not acquire the perfect source signal in practice. It is inevitable being mixed with RFI (Radio Frequency Interference) or undesired DC signal. Therefore, we could acquire the signal close to the real source signal with software correlator by massaging the received signal, with, e.g., a software filter. Thirdly, software correlator has more advantages in the respect of redesign. When the additional antennas are built, we can easily realize cross correlation between the newly built antennas and others.

We use C language to perform correlation. The library of Fastest Fourier Transform in the West (FFTW) is used for cross correlation, and CompuScope Software Development Kit (SDK) of Gage Instrument is used for interconnecting between the digitizer and PC. Additionally, Open Multi-Processing (OpenMP) in Intel Parallel Studio environment is used for parallel processing. In the beginning of development, we could collect data in about 0.8 sec due to the limitation of RAM size, but we need to collect longer for faint objects, such as Casiopeia A, and Crab Nebula. In order to detect the signal of the faint objects, we developed the program to conduct in pseudo-real time by using the parallel processing library, OpenMP. The block diagram of software correlator is illustrated in Fig. 16.
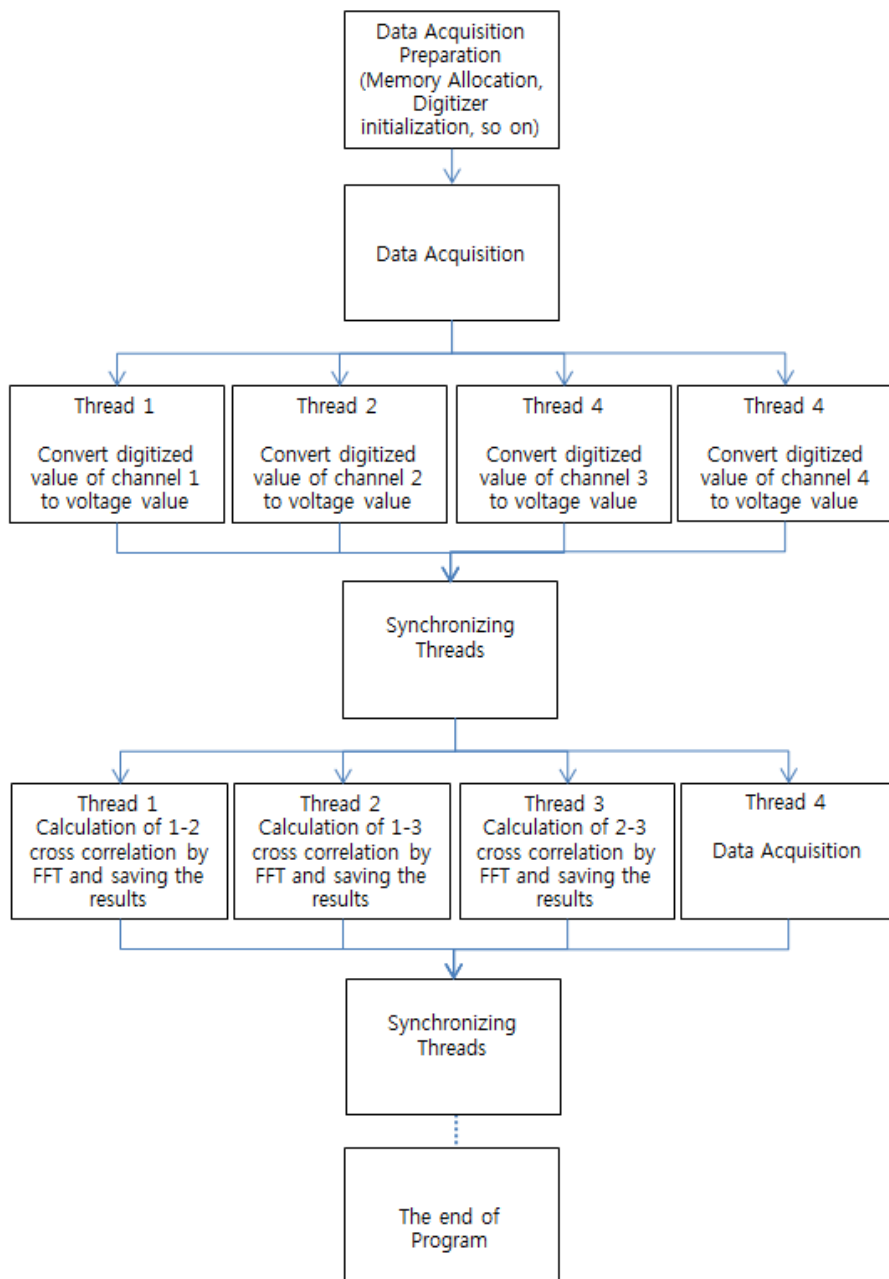
Fig. 16. Block Diagram of software correlator

2.5 Understanding of Signal Flow

The sample rate f_s must be at least twice the band limit ($B \leq f_s/2$) for perfect reconstruction by Nyquist-Shannon sampling theorem. The bandwidth of our receiver is 6MHz from 27MHz to 33MHz, so the sample rate f_s must be higher than at least 12MHz. Therefore, our digitizer, which has 50 M samples/s as the maximum sampling rate, can perfectly reconstruct the received signal. Possible center frequency could be calculated as below.

$$\frac{2f_H}{n} \leq f_s \leq \frac{2f_L}{n-1} \tag{2-1}$$

f_H, the highest frequency in our system, is 33MHz, f_L, the lowest frequency, is 27MHz and n is an integer. The highest n for which the condition is satisfied leads to the lowest possible sampling rates. Therefore, 20, 25, 50 M samples/s of the digitizer (refer to Table 2) are possible as the sampling rate.

Although undersampling does not affect signal reconstruction, we need to consider the effect of undersampling in analysis of signal flow. We will mathematically examine the effect of undersampling. We can let the signal before undersampling and the sampling pulse (50 MHz sampling rate) like

$$x(t) = cos(2\pi \, 30 \times 10^6 \, t + \theta) \tag{2-2}$$

$$p(t) = \sum_{n=-\infty}^{\infty} \delta(t - n\frac{1}{2\pi \, 50\times10^6}) \tag{2-3}$$

The signal after undersampling is the product of the signal before undersampling and the sampling pulse.

$$x_p(t) = x(t) \cdot p(t) \tag{2-4}$$

In order to define $x_p(t)$ in mathematical equation, using the Fourier Transform is easy to understand. The Fourier Transforms of them are

$$X(w) = \sqrt{2\pi} \frac{\delta(w - 2\pi\,30 \times 10^6) + \delta(w + 2\pi\,30 \times 10^6)}{2} e^{i\frac{\theta}{2\pi\,30 \times 10^6}w} \qquad (2\text{-}5)$$

$$P(w) = \sqrt{2\pi}\, 50 \times 10^6 \sum_{k=-\infty}^{\infty} \delta(w - 2\pi 50 \times 10^6\, k) \qquad (2\text{-}6)$$

$$X_p(w) = X(w) * P(w)$$

$$= \sqrt{2\pi}\, \frac{50}{2} \times 10^6 \sum_{k=-\infty}^{\infty}[\delta(w - 2\pi 50 \times 10^6\, k - 2\pi 30 \times 10^6) +$$

$$(w - 2\pi 50 \times 10^6\, k + 2\pi 30 \times 10^6)]\, e^{i\frac{\theta}{2\pi\,30 \times 10^6}(w - 2\pi 50 \times 10^6 k)} \qquad (2\text{-}7)$$

Let k=0, then sampled signal in frequency domain is

$$X_p(w) = \sqrt{2\pi}\, \frac{50}{2} \times 10^6 [\delta(w - 2\pi 30 \times 10^6\,)e^{i\frac{\theta}{2\pi\,30 \times 10^6}w} +$$

$$\delta(w + 2\pi 30 \times 10^6)e^{i\frac{\theta}{2\pi\,30 \times 10^6}w} \qquad (2\text{-}8)$$

x_p(t), the Inverse Fourier Transform of acquired $X_p(w)$, is

$$x_p(t) = 50 \times 10^6 \cos(2\pi\,30 \times 10^6\, t + \theta) \qquad (3\text{-}19)$$

It is derived that undersampling does not affect the data analysis process.

3. Test Observation and Data Analysis

3.1 Observation in Single Dish Mode

3.1.1 Receiver sensitivity

At first, we will find the antenna temperature of the Sun in our system. Recall that the Planck Law for blackbody radiation is

$$B_\nu = \frac{2h\nu^3}{c^2}\frac{1}{e^{h\nu/kT}-1} \tag{3-1}$$

Where B_ν is the specific intensity in $W/m^2/Hz/rad^2$, h is Planck constant, ν is the frequency in Hz, k is Boltzman constant, and T is temperature in K. At 12 GHz ($h\nu \ll kT$), an expansion of the exponential in Planck Law

$$e^{\frac{h\nu}{kT}} - 1 \cong 1 + \frac{h\nu}{kT} + \cdots \tag{3-2}$$

Results in

$$B_\nu = \frac{2\nu^2}{c^2}kT \tag{3-3}$$

This formula is Rayleigh-Jeans Law. With this equation, we will calculate the antenna temperature, when we observe the Sun by our system. For a uniform discrete radio source of temperature T, the source flux density in the Rayleigh-Jeans Law is

$$S = \frac{2\nu^2}{c^2}k\int_{\Omega_s} T(\theta,\phi)\,d\Omega = \frac{2\nu^2}{c^2}kT\Omega_s \tag{3-4}$$

where Ω_s is a solid angle of the source. The solid angle of the Sun is about 0.60×10^{-4} rad ($\Omega_s \sim \pi(0.25°)^2$). In aspect of the received antennas temperature (T_A), the received flux density is

$$\frac{1}{2}S = \frac{P}{A_e} = \frac{kT_A{}^*}{A_e} \tag{3-5}$$

where P is the power at the antenna terminals, and A_e is the effective aperture of the antenna, and T_A is the antenna

temperature. $\frac{1}{2}$ is the effect of polarization. Combining the two equations, (3-4), and (3-5), we could acquire approximate antenna temperature.

$$T_A{}^* = \frac{SA_e}{2k} = A_e \frac{v^2}{c^2} T\Omega_s = \frac{\Omega_s}{\Omega_A} T\eta_A \qquad (3\text{-}6)$$

The brightness temperature of the Sun is about 10^4 K, and the aperture efficiency η_A is approximately 0.7. Then, the antenna temperature of the Sun is about 2900K.

Now, we will derive the system temperature of our system. The power of the sky (P_{sky}) and the ambient (P_{amb}) are observed in order to measure the receiver sensitivity. Mountains are observed instead of the ambient. The measured data are displayed in Table 3. The following equation is used for the system temperature.

$$T_{sys} = \frac{T_{amb}}{\frac{P_{amb}}{P_{sky}} - 1} \cdot [1 + \frac{T_{amb} - T_{atm}}{T_{amb}}(e^\tau - 1)] = \frac{T_{amb}}{\frac{P_{amb}}{P_{sky}} - 1} \cdot CF \qquad (3\text{-}7)$$

The air is transparent at 12GHz, then, CF (correction factor) ~1 can be assumed. When the ambient temperature is assumed as 300 K, the system temperatures can be approximately calculated. The calculated system temperatures are displayed in Table 3. The system temperature is about 270 K overall.

The noise temperature of LNB at 25℃ is about 80K (1dB), and the noise temperature of the reflector is about 50K. If the efficiency of the passive devices between the reflector and LNB like a feed horn is 0.8, then the noise temperature is about 80K. Then, the total noise temperature is about 210K. Compared with the measured system temperature, 270K, this value, 210K, is reasonable when we consider the additional effect, like the atmosphere condition and the fact that the ambient is the mountain in practice.

With the derived system temperatures and the measured power of the Sun, the antenna temperatures of the Sun can be estimated. The measured powers of the Sun are described in Table 3. The source temperature is

$$T_A^* = \frac{P_{source} - P_{sky}}{P_{sky}} \, T_{sys} \qquad (3-8)$$

The calculated antenna temperatures of the Sun are respectively 2780, 2930, and 3231 K. These values are similar to the previously expected antenna temperature 2900 K.

Table 3. The power of ambient, the power of sky, receiver temperature, and system temperature at each antennas (2 PM, 29 December 2013)

	T_{amb} (~300K)	T_{sky}	T_{sun}	T_{sys}	T_A^*
Ant. 1	-25.2 dBm (=0.00302 mW)	-28.4 dBm (=0.00145 mW)	-17.2 dBm (=0.0190 mW)	277K	2780 K
Ant. 2	-23.9 dBm (=0.00407 mW)	-26.9 dBm (=0.00204 mW)	-16.6 dBm (=0.0219 mW)	301K	2930 K
Ant. 3	-27.4 dBm (=0.00182 mW)	-30.9 dBm (=0.000812 mW)	-19.3 dBm (=0.0117 mW)	241K	3231 K

3.1.2 Source detectability

When we make observation plan, we need to know the receiver sensitivity. Because the number of the antenna is only three, it is assumed that the sensitivity of the interference mode is similar

to the single dish mode in our system. Therefore, the noise uncertainties to an interferometer system are calculated as below

$$\Delta T_A = \frac{MT_{sys}}{\sqrt{t\Delta v}}$$ (3-9)

where M is a factor of order unity to explain extra noise due to ADC, and digital clipping, so on, Δv is bandwidth, and t is detection time. We found the system overall temperature in previous chapter. By using this value, about 260K, we can determine observable objects with our system. At first, we can calculate the minimum antenna temperature with some assumption, M ~ 1, t ~ 1 sec (we observe objects during 1 sec), and Δv ~ 6 MHz (our receiver characteristics). When the values, M, t, Δv, and T_{sys} are substituted in equation (3-9), the minimum antenna temperature is 0.11 K. Usually, the brightness of radio sources are not described with temperature, but flux density, so we need to convert from antenna temperature to flux density. We use the relation equation between antenna temperature and flux density, which is

$$P = kT_{sys} = \frac{1}{2}A_{eff}S$$ (3-10)

where k is Boltzmann constant, A_{eff} is the effective cross section of the antenna dish, and S is flux density. It can be assumed that efficiency of the antenna is about 0.7, then, A_{eff} is about 2.29m^2 (1.8^2 x 0.7). Then, when we conduct observation during 1 sec, the minimum flux density is about 133 Jy.

When we observe some objects with our receiver during 1 sec, we can observe the objects which have higher flux density than 133Jy at 12 GHz. Therefore, we can probably observe the Sun, Moon, Cassiopeia A, Cygnus A, Orion KL Nebula, and Crab Nebula among the objects of Fig. 17. We selected the Sun, Moon as the target to make the image, and Cassiopeia A, Crab Nebula as the

phase calibrator. However, Cassiopeia A and Crab Nebula are a little ambiguous, because their sizes are similar to the maximum resolution. The size of Cassiopeia is about 5′ and Crab Nebula is about 7′.
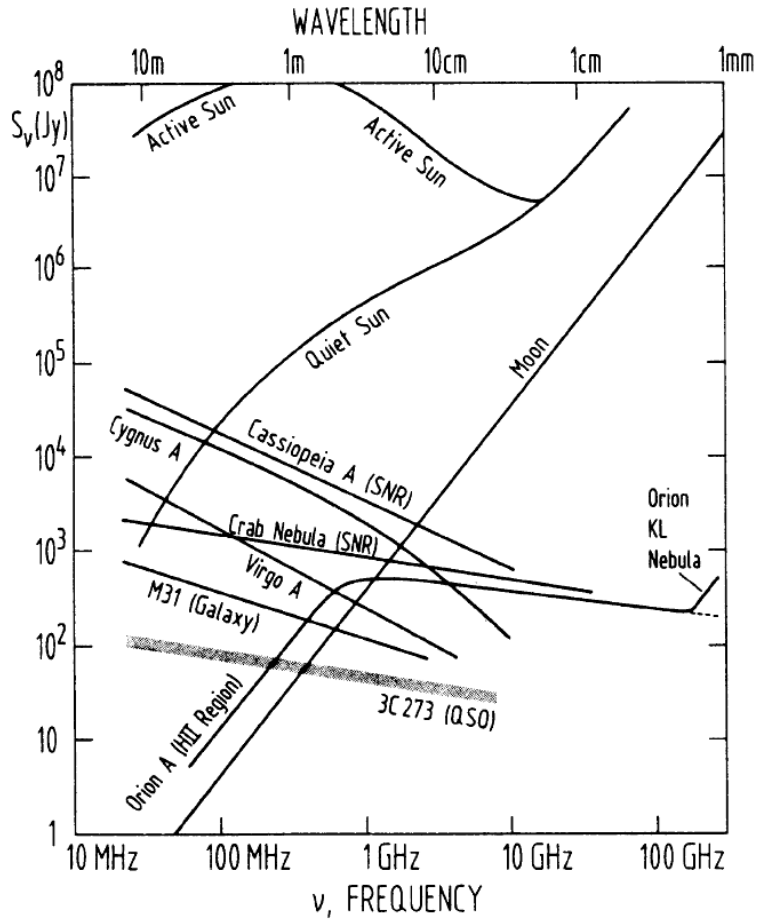

Fig. 17. The spectral distributions of various radio sources (Wilson et al. 2009)

3.2 Fringe Detection

We succeed in detecting the fringe of the Sun, Moon, Cassiopeia A, and Crab Nebula. Fig. 19 is the fringe of the Sun at 5 April 2014. It shows that the strength of 1-2 cross correlation is stronger than others. The reason why 1-2 cross correlation has the strongest visibility amplitude is that the sun is an extended source and 1-2 baseline length is the shortest. The relation between visibility and baseline length of a Gaussian extended source is based on Gaussian function (Fig. 18. a), so the 1-2 visibility of the Sun with the shortest baseline length has the largest amplitude. The visibility of other pairs also was detectable due to the strong flux of the Sun. Fig. 19 shows the visibilities of 1-2, 1-3, and 2-3. The maximum visibility point is approximately located near 0 time delay.
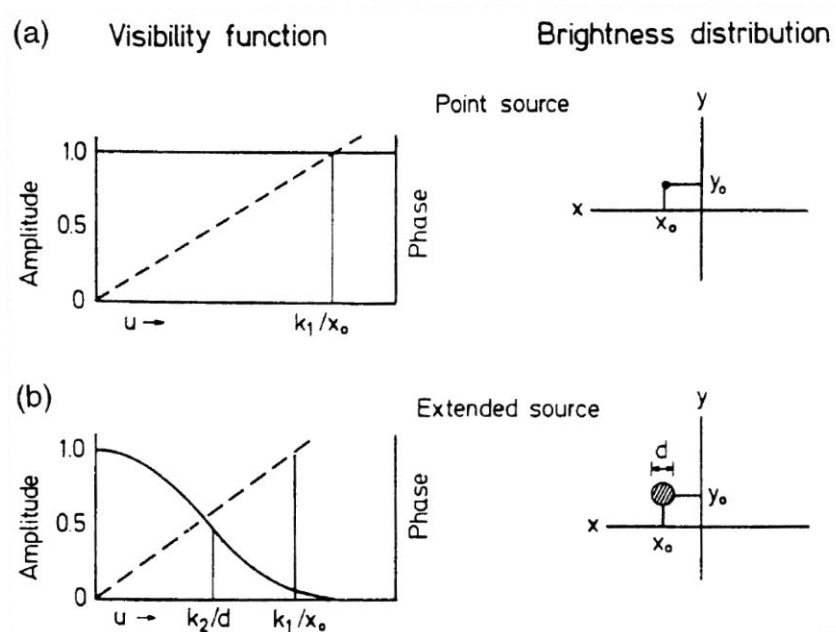

Fig. 18. The visibility functions for a point source (a) and a Gaussian shaped extended source (b) (T.L. Wilson et al. 2009)
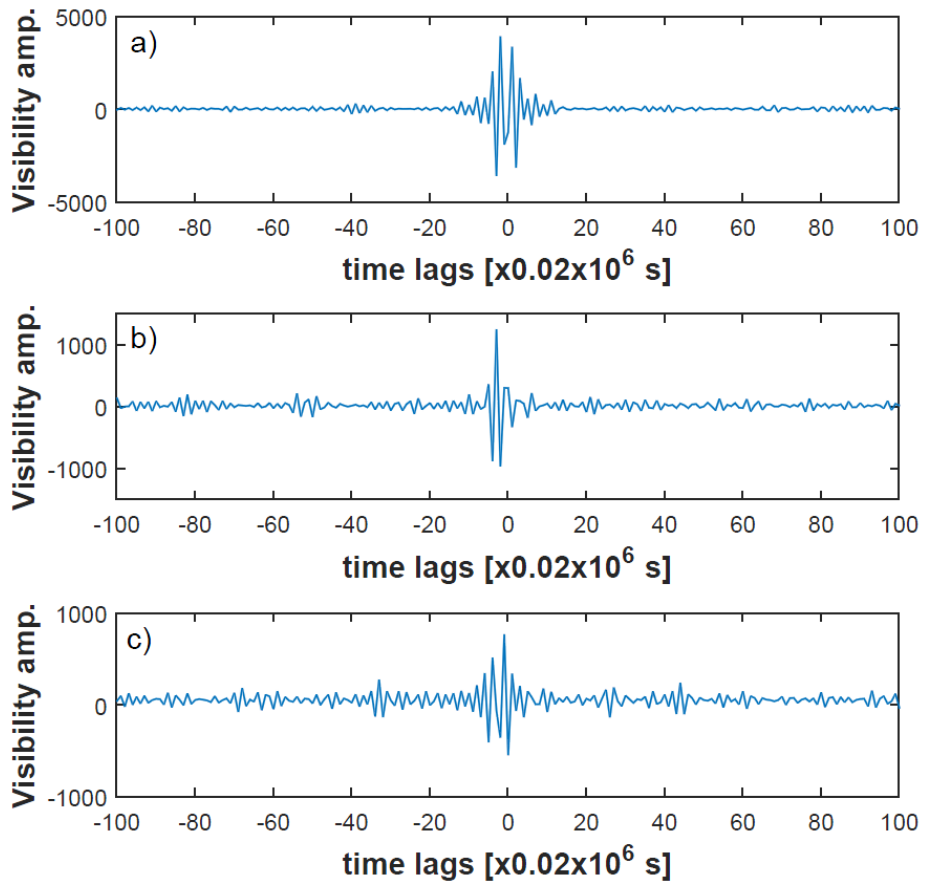
Fig. 19. 1-2(a), 1-3(b), 2-3(c) visibilities of the Sun

In order to secure that the observed fringes are true fringes, not the RFI, it is necessary to check the visibility variation affected by the variation of geometric delay along with time. Varying the observation time, the geometric delay changes, thus the fringe is shifted. Shift direction depends on the variation of the geometric delay. Fig. 20 shows the visibility variation from up to down or from down to up due to the shift of the fringe. The data is observed at 19 February 2014 and the observed times are captioned in Fig. 20. In order to calculate geometric time delay, the fringes must be fitted. Our system is upper sideband heterodyne, so the used visibility fitting equation is

26

$$r_u = A\Delta v|V|\frac{sin[\pi\Delta v(\tau_g-\tau_i)]}{\pi\Delta v(\tau_g-\tau_i)}cos\{2\pi(v_{LO}\tau_g + v_{IF}(\tau_g-\tau_i)\} - (\phi_V + \phi_{LO})]$$

(3-11)

where |V| is the amplitude of the visibility, Δv is the IF bandwidth, τ_g is the geometric delay, τ_i is the instrumental delay, v_{LO} is the local oscillator frequency, and v_{IF} is the center frequency of the IF band. ϕ_V is the phase of visibility, and ϕ_{LO} is any phase difference between the local oscillator signals of two antennas. With the equation (3-11), the geometric time delay could be expected, and the expected geometric time delay is shown in Fig. 21. The used data is 1-2 visibility. Even though the visibility also include phase information of local oscillator and visibility phase, the phase of 1-2 visibility, $(\phi_V + \phi_{LO})$, is predicted to be almost constant because 1-2 baseline is very short, so acquired delay is expected to be almost affected by the geometric delay. The variation of geometric time delay could be observed during the time variation like Fig. 21, and this aspect is almost attributed to the geometric time delay.
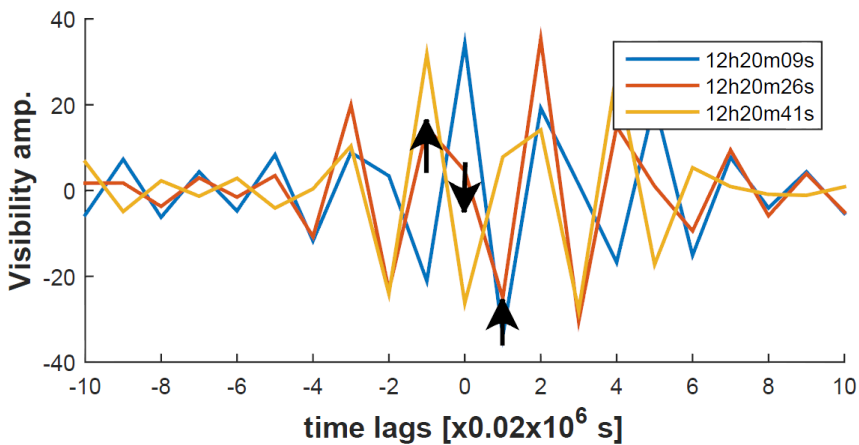

Fig. 20. The visibility variation of 1-2 pair during time variation (19 February 2014)
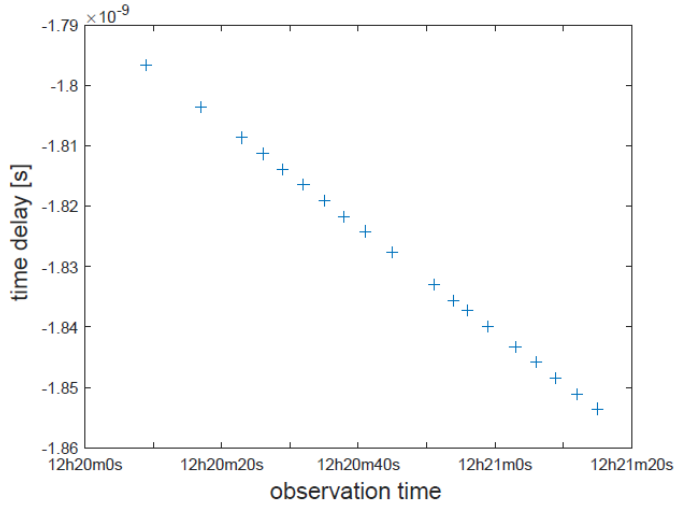
27

Fig. 21. The time delay variation during the observation time (19 February 2014)

We also observed the point sources, Crab nebula, and Cassiopeia A. However, we could not find visibilities for all pairs. We could acquire only 1-2 visibility like Fig. 22. At the present time, the reason why all visibilities cannot be found is unclear. However, we speculate the difficulties to make specific mount model, and unidentified receiver sensitivity problems. In addition, Crab nebula and Cassiopeia A are not really point sources as explained in chapter 3.1.2. This is the most likely reason that we can think of.
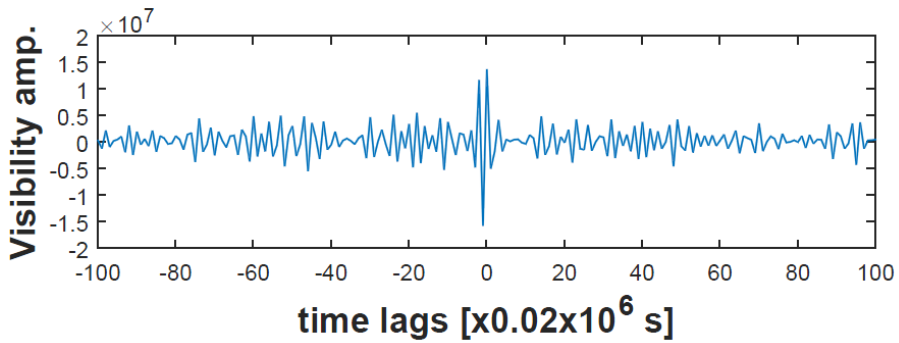

Fig. 22. 1-2 Visibility of Crab Nebula at 5 June 2014

3.3 Imaging of the Sun

We acquired the visibility of the Sun. Using the acquired amplitude and phase information by the visibility fitting equation, we could make the synthesized source image.

3.3.1 UV coverage

In order to make the synthesized image, we used the observation data of the Sun at 12 February 2014, which has 18 points during one day. The Nobeyama 17 GHz radio image of the sun taken at the same day exhibits a simple structure with a bright spot at the center. We analyze these data because the simple and symmetric image may give hints for eliminating the involved unknown cable length differences. We make the UV coverage (Fig. 23) with observed times and the location of the antennas (Fig. 5). As expected, UV coverage has 36 data points which have short baseline, and 72 data points which have long baseline.
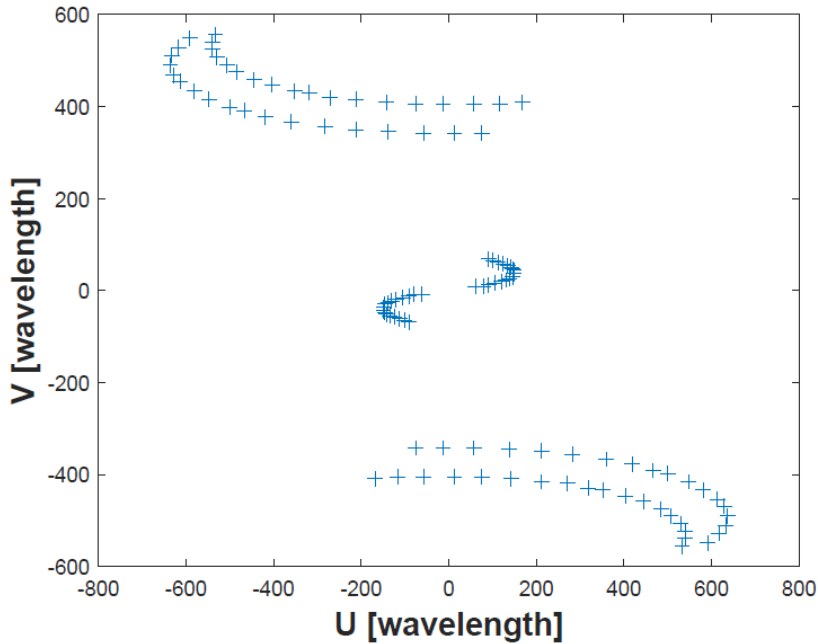

Fig. 23. UV coverage at 12 February 2014 (18 points)

3.3.2 Visibility equation and data fitting

In order to acquire the visibility amplitude and phase, the equation (3-13) is used. In our system, the IF bandwidth ($\Delta \nu$) is 6MHz, the local oscillator frequency (ν_{LO}) is 12.147GHz, and the center frequency of the IF band (ν_{IF}) is 30MHz. An addition of a constant term (ϕ_{LO}) to ϕ_V does not affect image, so $\phi_V + \phi_{LO}$ is used. The representative fitted results of each pairs are shown in from Fig. 24 to Fig. 26. Blue dots are the detected value, the solid line is the fitted line, and the dotted lines are the bounded line at 99%. Through the fitting model, we could acquire the amplitude and phase values of the visibility.
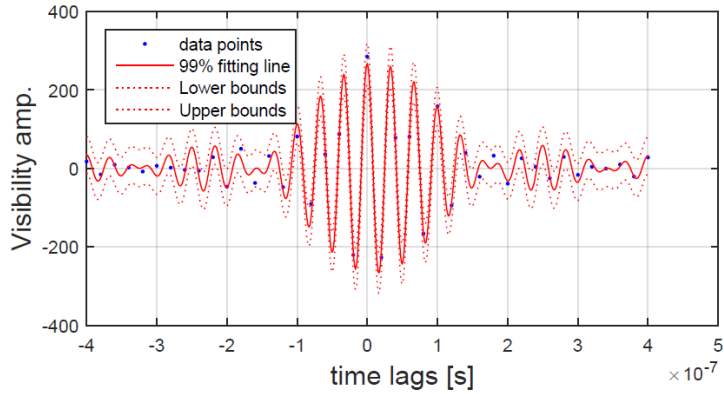

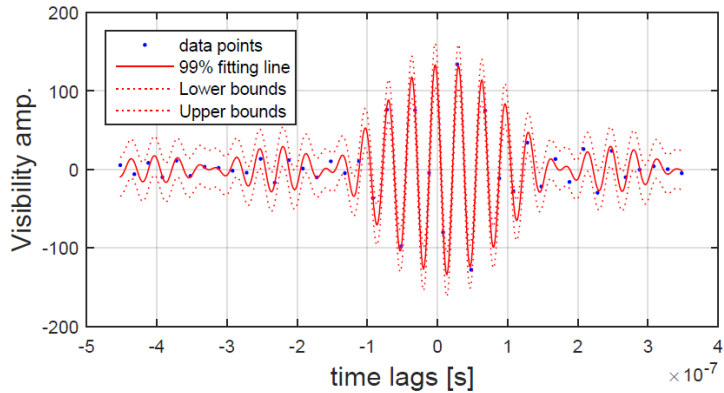**Fig. 24.** Cross-correlation between 1 antenna and 2 antenna

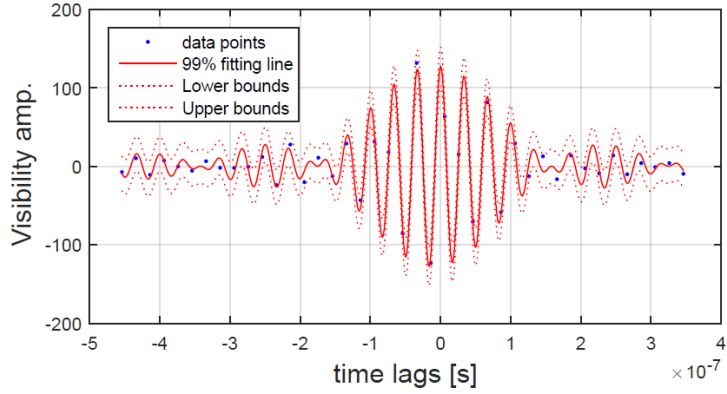**Fig. 25**. Cross-correlation between 1 antenna and 3 antenna

Fig. 26. Cross-correlation between 2 antenna and 3 antenna

3.3.3 Non-imaging data analysis

Before making the synthesized image, the visibility amplitude is derived as a function of baseline length. Assuming that the feature of the 12 GHz Sun observed by our system is similar to the 17 GHz Sun which observed by Nobeyama Solar Radio Telescope (Fig. 27), the Sun has disk-like brightness distribution with one sunspot at the center. With this assumed feature of the Sun, we can calculate the visibility amplitude function as the baseline length. The expected visibility is the sum of a constant due to the sunspot at the center and the Bessel function due to the disk-like distribution. However, most flux is contributed by the disk-like structure, so the constant value is expected to be very smaller than the value by solar disk. The expected visibility is described as the solid line, and the data points are described as the cross in Fig. 28. As expected, measured visibility amplitudes approach well to the expected visibility values. From this result, we could guess that the size of the 12 GHz Sun is about 36′. This value is a little lager than the optical size of the Sun, 30′. However, when we consider the effect of the radio microwave and the limitation of the assumed discrete image (about 2′ is one pixel), this value is reasonable.
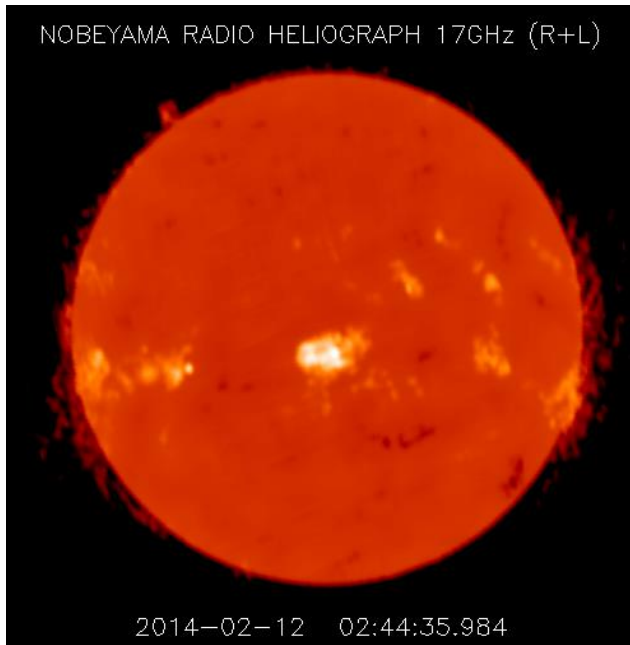
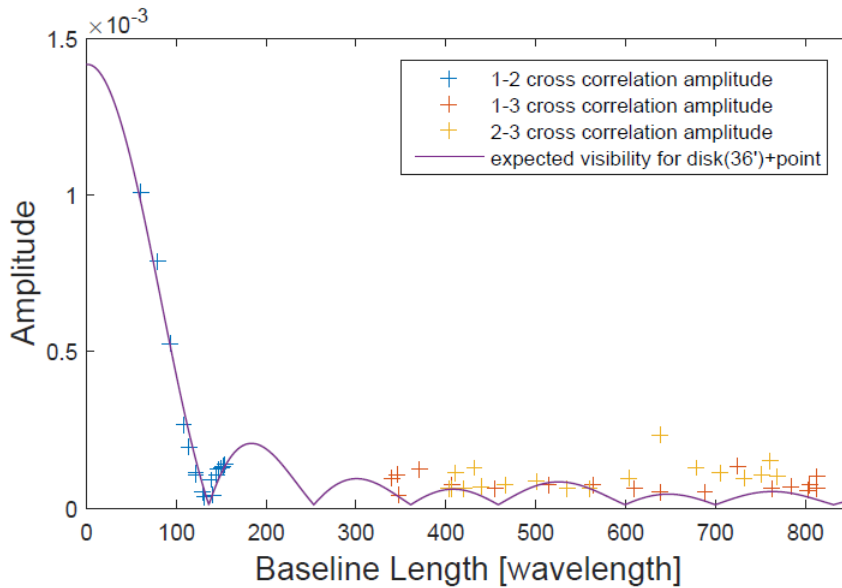**Fig. 27.** The 17 GHz Sun image at 12 February 2014 which is observed by Nobeyama Solar Radio telescope

Fig. 28. Visibility amplitude is displayed as a function of baseline length. Crosses are the acquired data, and solid line is the expected visibility amplitude of 36′ disk and the sunspot. The ratio of the disk amplitude to the sunspot is about 40.

As mentioned in the previous chapter, we could not detect all fringes of point sources, so self-calibration is necessary to correct the phase information. Before conducting self-calibration, the initial model of the Sun is made. The model is expected by the image of the 17GHz Sun, which is observed by Nobeyama Solar Radio Telescope (Fig. 27). The modeled phase of the pairs is expected as almost constant, because the phase of 2 dimensional Fourier transform about a point source is constant, and the visibility phase of the disk-like extended source at the center is also constant. As expected, the phase of 1-2 pair is almost constant as shown in Fig. 29, so we could find ϕ_{LO} ~ 0.1109 rad. However, the phases of other pairs spread widely in the range of $[0, 2\pi]$. It seems that the phases of 1-3 and 2-3 pair are not constant. Therefore, we could not find ϕ_{LO} of 1-3 and 2-3 pair and not make image using a conventional way. The observation and self-calibration of Moon which has smooth structure or the observation of phase calibrators seems necessary for finding ϕ_{LO}.
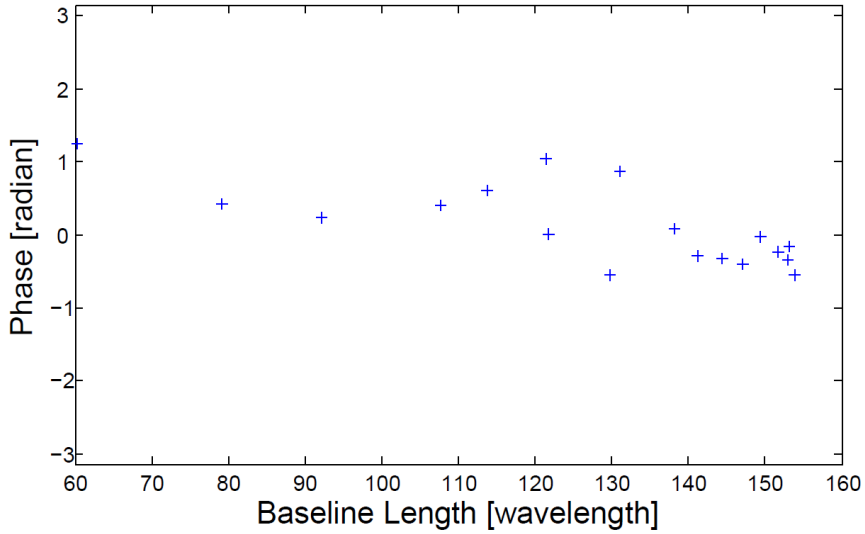

Fig. 29. The phase of 1-2 pair

3.3.4 Synthesized image

Although we could not find the specific phase information of 1-3 and 2-3 pair, we made synthesized image with limited information (Fig. 30). Comparing with the UV coverage (Fig. 23), we can expect that the extended structure of the Sun could be appeared in the horizontal direction and the compact structure in diagonal direction from upper-left to lower-right. This characteristic is well shown in Fig. 30. In order to test the fidelity of this image, we made an image using visibilities of solar disk model, but sampled at the observed UV positions. This image is displayed in Fig. 31. The extended structure of the synthesized image is similar to the simplified model image (Fig. 31) because the information of 1-2 pair is almost exact. However, the compact structure is different due to the unclear phase information.
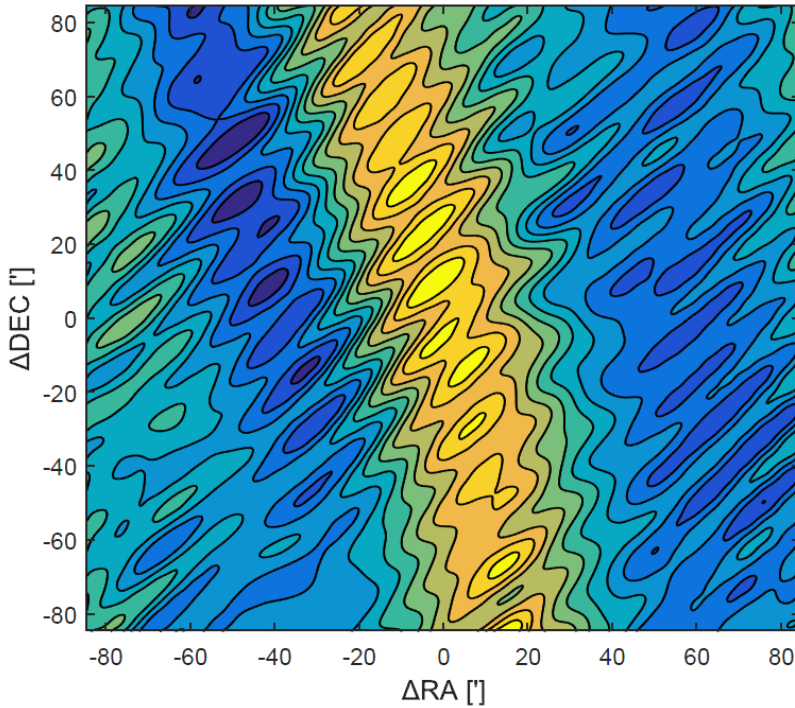

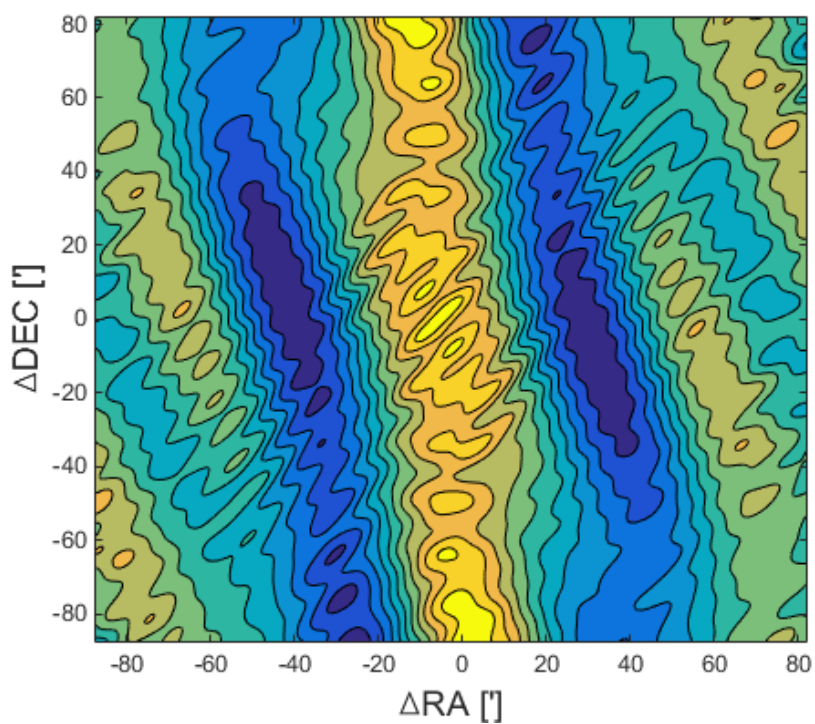**Fig. 300.** Synthesized image of the Sun.

Fig. 31. The image of the solar disk model, synthesized with the
visibilities sampled at the observed UV positions

4. Discussion

We developed the Goheung interferometer system and succeed in acquiring the signal of the Sun, Moon, and Crab Nebula. However, we did not derive the visibilities for all pairs in the observation of point sources, Crab Nebula and Cassiopeia A. We think that the reasons are the difficulties to make specific mount model, unidentified receiver problems, or they are not really point sources. Therefore, we could not calibrate the complex visibilities in phase.

However, the observed antenna temperatures of the Sun are well derived with the expected antenna temperatures. In addition, the time variation of the visibility, which is the firm evidence of the signal detection, is well observed. With well observed visibilities, the amplitude and phase of the complex visibility are calculated by fitting model. The relation found between the acquired visibility amplitude and baseline length is very similar to the visibility amplitude, Bessel function plus a constant, expected for disk-like structure and point source at the center. The synthesized solar image is obtained from the fitted amplitudes and phases.

We could understand the principle of single dish telescope, interferometer system, and the data analysis process.

5. Reference

Arndt Martina B.; Rogers Alan E. E., 2009, 'VSRT Introduction'

Breen, S. L.; Ellingsen, S. P.; Caswell, J. L.; Green, J. A.; Voronkov, M. A.; Fuller, G. A.; Quinn, L. J.; Avison, A., 2012 '12.2-GHz methanol maser MMB follow-up catalogue –I. Longitude range 330° -10°', MNRAS, 426, 1703

Evarts, E. R.; Rogers, A. E.; Pratap, P. 2005, 'Using Small Radio Telescopes for Very Long Baseline Interferometry', American Astronomical Society, 2005AAS...207.6608E

Oppenheim, Alan V.; Willsky, Alan S.; Hamid, S., 2000, 'Signals and Systems', Second Edition, Prentice Hall

Park, Y.-S. et al., 2006, 'Development of Semi-VLBI System and Observation of Sun at 21 cm', JKAS, 39, 51

Park, Y.-S. et al., 2008, 'Development of a Toy Interferometer for Education and observation of Sun at 21cm', JKAS, 41, 77

Taylor, G. B.; Carilli, C. L.; Perley, R. A. 2007, 'Synthesis Imaging in Radio Astronomy II', Astronomical Society of the Pacific Conference Series Volume 180

Wilson, T. L.; Rohlfs, K.; Huttemeister, S., 2009, 'Tools of Radio Astronomy', Fifth Edition, Spring

초 록

교육과 연구를 위한
12 GHz 전파 간섭계 개발

국립고흥청소년우주체험센터를 방문하는 학생들의 교육과 연구를 위해 12GHz 전파 간섭계를 개발했다. 저비용으로 제작하기 위하여 상용 제품들을 주로 사용하였고, 해변가에 위치한 센터 특성상 강한 바람을 견디도록 구동계를 설계, 제작 하였다. 고흥 간섭계는 직경 1.8m 의 off-axis 포물면 안테나 3 대로 이루어져 있으며, 각 안테나 사이의 기선길이는 4m, 19m, 20m 로, 약 4′의 분해능을 가지는 영상을 얻을 수 있다. 수신기는 중심 주파수 12.177GHz, 대역폭 6MHz 이어서 태양, 달, 은하면에서 나오는 메탄올 스펙트럼과 연속파를 관측할 수 있다. 각 수신기에서 나오는 신호는 digitizer 로 읽어 들이며, 개발된 병렬 처리 프로그램을 통하여 software correlation 을 수행한다. 태양, 달, Crab Nebula, Cassiopeia A 등을 관측하여 프린지를 검출하는데 성공하였다. 일본 Nobeyama Solar Radio telescope 로 관측한 17 GHz 대역의 원반 중심에 밝은 점 전파원이 있는 태양 이미지를 이용하여 신호선의 길이차이를 보정하는 calibration 을 시도하였으나 짧은 기선에서만 유효한 것으로 보인다. 추후 별도의 위상 보정 천체를 이용하거나, 이것 없이 self-calibration 과 비슷한 방법으로 태양 이미지를 만드는 알고리즘을 개발할 필요가 있다.

주요어 : 간섭계, 12 GHz, 교육

학 번 : 2012-23106